Midlatitude atmospheric OH response to the most recent 11-y solar cycle

Shuhui Wang[a,1], King-Fai Li[b,c], Thomas J. Pongetti[a], Stanley P. Sander[a], Yuk L. Yung[b], Mao-Chang Liang[d], Nathaniel J. Livesey[a], Michelle L. Santee[a], Jerald W. Harder[e], Martin Snow[e], and Franklin P. Mills[c,f]

[a]Jet Propulsion Laboratory, California Institute of Technology, Pasadena, CA 91109; [b]Division of Geological and Planetary Sciences, California Institute of Technology, Pasadena, CA 91125; [c]Atomic and Molecular Physics Laboratories, Research School of Physics and Engineering, and [f]The Fenner School of Environment and Society, Australian National University, Canberra, ACT 0200, Australia; [d]Research Center for Environmental Changes, Academia Sinica, Taipei 115, Taiwan; and [e]Laboratory for Atmospheric and Space Physics, University of Colorado, Boulder, CO 80303

Edited* by Steven C. Wofsy, Harvard University, Cambridge, MA, and approved December 19, 2012 (received for review November 1, 2011)

The hydroxyl radical (OH) plays an important role in middle atmospheric photochemistry, particularly in ozone (O_3) chemistry. Because it is mainly produced through photolysis and has a short chemical lifetime, OH is expected to show rapid responses to solar forcing [e.g., the 11-y solar cycle (SC)], resulting in variabilities in related middle atmospheric O_3 chemistry. Here, we present an effort to investigate such OH variability using long-term observations (from space and the surface) and model simulations. Ground-based measurements and data from the Microwave Limb Sounder on the National Aeronautics and Space Administration's Aura satellite suggest an ∼7–10% decrease in OH column abundance from solar maximum to solar minimum that is highly correlated with changes in total solar irradiance, solar Mg-II index, and Lyman-α index during SC 23. However, model simulations using a commonly accepted solar UV variability parameterization give much smaller OH variability (∼3%). Although this discrepancy could result partially from the limitations in our current understanding of middle atmospheric chemistry, recently published solar spectral irradiance data from the Solar Radiation and Climate Experiment suggest a solar UV variability that is much larger than previously believed. With a solar forcing derived from the Solar Radiation and Climate Experiment data, modeled OH variability (∼6–7%) agrees much better with observations. Model simulations reveal the detailed chemical mechanisms, suggesting that such OH variability and the corresponding catalytic chemistry may dominate the O_3 SC signal in the upper stratosphere. Continuing measurements through SC 24 are required to understand this OH variability and its impacts on O_3 further.

decadal variability | odd hydrogen

Quantifying effects of the solar cycle (SC) in Earth's atmosphere helps differentiate relative contributions of natural processes and anthropogenic activities to global climate change (1). From the 11-y SC maximum (max) to minimum (min), the total solar irradiance (TSI) varies only by ∼0.1%. However, changes in solar UV fluxes can be much larger (2). Thus, detectable SC impacts on Earth's climate are more likely to be linked to changes in middle (stratosphere and mesosphere, tropopause to ∼90 km) and upper (thermosphere and above) atmospheric composition through photochemistry in the UV region.

A number of observational and modeling studies have characterized SC modulations in mesospheric and stratospheric chemistry, especially in ozone (O_3) (3–9). Changes in UV absorption by O_3 at low latitudes over the SC can lead to changes in thermal structures in the middle atmosphere, affecting tropospheric and polar climates, and may lead to changes in global circulations (1). Accurate simulations of the O_3 response to the SC are therefore required for better understanding the sun-climate relationship (10, 11). However, the SC signal in O_3 simulated by different models shows quantitative differences, which may be due to differences in model resolutions, model parameterizations related to dynamical processes, and/or photochemistry that has not yet been critically examined (12, 13). Diagnostic studies must involve not only O_3 but species that catalytically destroy O_3, such as odd-hydrogen (HO_x) [HO_x = H + OH (hydroxy radical) + HO_2 (hydroperoxyl)] (14–19).

OH, in particular, is a key species in HO_x reaction cycles. It is mainly produced through direct photolysis of water vapor (H_2O) at ∼120 and 170–205 nm and photolysis of O_3 at ∼200–330 nm, followed by reaction of $O(^1D)$ with H_2O (20). Due to its short chemical lifetime, rapid response of OH to the SC can serve as a good indicator of solar-induced changes in atmospheric composition and chemistry. Unfortunately, very few studies have been performed on the HO_x response to the SC, and little attention has been paid to the impacts of such changes on O_3 (15). Furthermore, recent observations over the declining phase of SC 23 by the Solar Stellar Irradiance Comparison Experiment (SOLSTICE) (21) and the spectral irradiance monitor (SIM) (22) instruments aboard the Solar Radiation and Climate Experiment (SORCE) satellite suggest an unexpectedly large decrease in solar UV irradiance, which has important implications for O_3 and HO_x photochemistry (5). These observations, particularly the solar irradiance data from the SIM, disagree with previous satellite observations and model parameterizations, adding UV variability as another dimension of uncertainty for atmospheric modeling.

The objectives of the present work include the following: (*i*) providing observational evidence of SC-related changes in OH column abundance (X_{OH}) from 15 y of ground-based measurement, augmented by 5-y satellite OH measurements by the Microwave Limb Sounder (MLS) aboard the National Aeronautics and Space Administration's (NASA) Aura satellite; (*ii*) quantifying the impacts of using SORCE UV variability on X_{OH} SC variability with a 3D Whole Atmosphere Community Climate Model (WACCM) (2) and a 1D photochemical model (23); and (*iii*) estimating the sensitivity of stratospheric O_3 to the SC-related OH changes obtained in *ii*. Note that previous studies on the O_3 response to the SC investigate the overall O_3 variability due to chemistry, dynamics, and radiation. Our objective in *iii* is to illustrate the role of OH in the SC modulations of O_3 chemistry.

This study uses long-term OH measurements from space and the surface to investigate the OH response to the SC, providing a basis for simulating long-term variability of HO_x chemistry in the middle atmosphere.

Author contributions: S.W., K.-F.L., S.P.S., Y.L.Y., and F.P.M. designed research; S.W., K.-F.L., and T.J.P. performed research; M.-C.L., J.W.H., and M.S. contributed new reagents/analytic tools; S.W., T.J.P., N.J.L., M.L.S., J.W.H., and M.S. analyzed data; and S.W. and K.-F.L. wrote the paper.

The authors declare no conflict of interest.

*This Direct Submission article had a prearranged editor.

[1]To whom correspondence should be addressed. E-mail: shuhui.wang@jpl.nasa.gov.

This article contains supporting information online at www.pnas.org/lookup/suppl/doi:10.1073/pnas.1117790110/-/DCSupplemental.

Observational Evidence

Studies on SC modulations of OH have been limited in the past by the lack of long-term systematic observations. The only two long-term records are X_{OH} measurements at the NASA Jet Propulsion Laboratory's (JPL) Table Mountain Facility (TMF) in California (24) and at the National Oceanic and Atmospheric Administration's (NOAA) Fritz Peak Observatory (FPO) in Colorado (25). Based on FPO X_{OH} data during 1977–2000, an X_{OH} variability of ±4.2% (or 8.4% peak to valley) was derived and attributed to the 11-y SC (15). A trend suggestive of a similar SC response in TMF X_{OH} data during 1997–2001 was also reported (17), but the robustness of such analysis was limited by the short period of the observations. In this study, we update TMF X_{OH} data to 1997–2012, covering most of SC 23 and the rising portion of SC 24.

X_{OH} is measured by a high-resolution Fourier Transform UV-visible Spectrometer (FTUVS) at the TMF at an altitude of ~2.3 km in Wrightwood, California (34.4° N, 117.7° W) (24). The FTUVS makes diurnal X_{OH} measurements during daytime. Two dominant natural variabilities of OH are the diurnal cycle due to the change of solar zenith angle (SZA) over the course of a day and the seasonal cycle, which is a combined effect of varying SZA and sources of OH (26). To focus on the SC signal, we first minimize the diurnal effect by using daily max (Fig. 1*A*) determined by a polynomial fit of the diurnal pattern (*SI Text*). The average time of daily max is close to 20:00 Universal Time (UT; local noon). To minimize the seasonal effect, we applied a fast Fourier transform (FFT) low-pass filter to the X_{OH} daily max (details are provided in *SI Text*). The result of 2-y FFT filtering (removing variations with frequencies higher than once every 2 y) is selected to represent the long-term variability that is primarily due to the SC (Fig. 1*A*, red line). Further FFT filtering smears the SC signal, whereas less FFT filtering retains additional interannual features that are not related to the SC (e.g., 1-y FFT filtering is shown in Fig. 1*A*, green line). The FFT results are normalized by the all-time mean X_{OH} (Fig. 1*C*). TMF X_{OH} SC variability is found to be ~10% from peak to valley. We also applied a regression analysis (9) using the long-term Lyman-α index as a proxy for the SC (*SI Text*). The result is consistent with the FFT analysis (Fig. 1*C*, gray), with an uncertainty of ±3% (1σ). This OH variability agrees with that observed over the FPO (15), although the absolute values of X_{OH} from the FPO and TMF, both in middle latitudes, have shown statistical differences of several tens of percentage points (27).

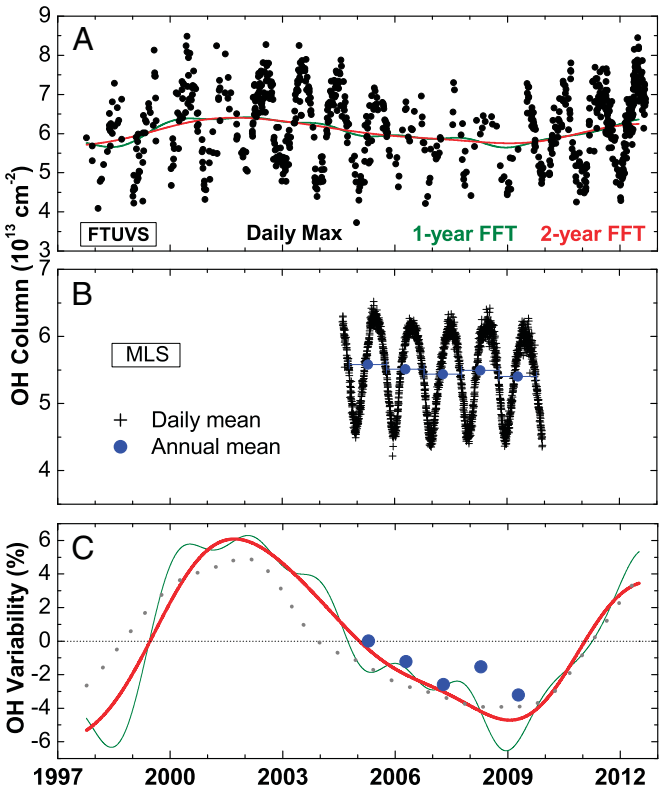

Fig. 1. Daily max OH column at the TMF and its SC variability. (*A*) Daily max FTUVS X_{OH} (black) and its long-term variability based on the FFT (red and green). (*B*) Daily mean (black) and annual mean (blue) MLS X_{OH} values around the TMF latitude. (*C*) Long-term FTUVS X_{OH} variability normalized to an all-time mean (red and green, from FFT; gray, from regression) and the comparable variability in MLS X_{OH} (blue).

Since the launch of Aura in July 2004, daily global OH distribution has been measured by the MLS (28). Excellent data quality has been demonstrated through extensive validations with airborne and ground-based measurements and modeling (29–31). Nearly continuous MLS OH data are available from 2004 (middle of the declining phase of SC 23) to the end of 2009 (start of SC 24). To compare these data with FTUVS data, we focus on the MLS OH at TMF latitude (29.5° N to 39.5° N). Data between 21.5 and 0.0032 hectopascal (hPa) are integrated to give an estimate of X_{OH}, which covers ~90% of the total atmospheric OH (31). Such integration is expected to include most of the SC signal. Furthermore, the average MLS overpass time at the TMF is ~21:00 UT (31), making MLS X_{OH} close to TMF daily max X_{OH} (~20:00 UT). Fig. 1*B* shows the zonal mean daily MLS X_{OH} over the TMF and the annual average, in which the seasonal variation is removed. The first year mean (August 2004 to August 2005) is used to normalize the annual mean X_{OH} to obtain the relative variability (Fig. 1*C*, blue), which is primarily due to the SC, with small additional interannual variations. The resulting trend is in good agreement with that of TMF X_{OH}, although only five annual mean MLS data points are available and the slightly high MLS X_{OH} during 2007–2008 may require further investigation. Between 2004 and 2009, the MLS annual mean X_{OH} decreased by over 3%. Based on the scale of TMF X_{OH} variability, we estimate the total SC signal in MLS X_{OH} to be ~7–8%, within the uncertainty range of the SC signal in TMF X_{OH}.

As a robustness test, the X_{OH} SC signals obtained above are compared with observations of various solar parameters (Fig. 2). Independent TSI measurements have been provided by a number of satellite instruments since 1978. Based on these observations, various versions of the TSI composite have been constructed [e.g., ACRIM, primarily using data from three generations of the Active Cavity Radiometer Irradiance Monitor (32); PMOD, from the Physikalisch-Meteorologisches Observatorium Davos World Radiation Center (33)]. These composites, as well as the most recent TSI measurement (2003–2012) by the Total Irradiance Monitor (34) aboard the SORCE, are plotted in Fig. 2*A*. Despite quantitative differences between ACRIM and PMOD data, which may be due to uncorrected instrumental drifts (35), both composites clearly demonstrate a prolonged solar min near the end of SC 23. To remove the short-term variability, the SORCE TSI is annually averaged and the composites are smoothed. The extracted SC signals in X_{OH} show good correlation with the SORCE TSI (Fig. 2*B*) and generally follow the TSI composites (Fig. 2*C*), with some differences in the ascending phase of SC 23. Although the TSI is a good indicator of the integrated solar spectrum variability, short-wavelength UV radiation may vary differently from longer wavelength radiation. Therefore, we also compare the observed X_{OH} variability with those in the solar Lyman-α index at 121.5 nm and the Mg-II index near 280 nm (composites from the Laboratory for Atmospheric and Space Physics Interactive Solar Irradiance Datacenter based

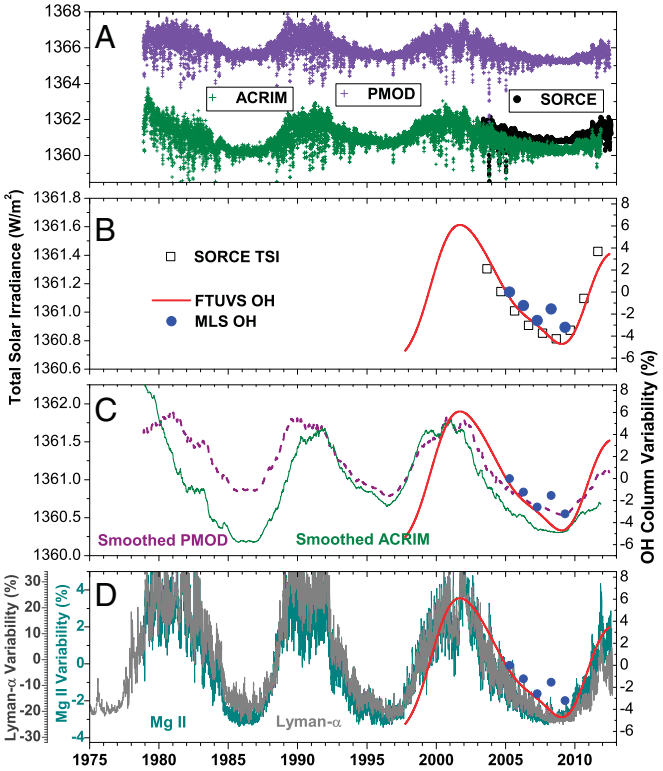

Fig. 2. OH SC variability correlates well with solar parameters. (*A*) Daily mean TSI from the SORCE (black), PMOD composite (purple), and ACRIM composite (green). (*B*) FTUVS (red) and MLS (blue) X_{OH} variability (Fig. 1) in comparison to variability in annual mean SORCE TSI (black). (*C*) Same as in *B*, but replacing SORCE TSI with smoothed ACRIM and PMOD composites. The PMOD TSI was adjusted by 4.7 W/m^2. (*D*) X_{OH} variability in comparison to variabilities in Lyman-α (gray) and Mg-II (cyan) indices.

on multiple satellite measurements), which are proxies for solar UV variations. They both correlate well with the observed X_{OH} variability over SC 23 (Fig. 2*D*).

Model Results and Discussion

We simulated the SC modulation in X_{OH} with the WACCM, a 3D global atmospheric model extending from the surface to ~140 km (2). The advantage of using the WACCM is that chemistry, radiation, and dynamics are fully coupled, providing a comprehensive simulation of SC effects on X_{OH} at middle latitudes. Four 50-y-long WACCM runs with different prescriptions of solar UV variability (described below) were carried out.

Most climate models with prescribed solar forcing use a parameterized solar spectral irradiance (SSI) variability developed at the Naval Research Laboratory (NRL), which is primarily based on space-borne UV measurements during 1991–2000 (36). Fig. 3*A* shows the simulated annual mean X_{OH} from 1964 to 2010 using this NRL solar forcing. The TMF and MLS X_{OH} values are represented by model OH integrated from the upper mesosphere down to 2.3 km and 25 km, respectively. The average SC signal in X_{OH} is only ~3% from max to min, suggesting differences of a factor of ~3 between the model and observations (Fig. 3*B*). Note that another run with the standard WACCM SC setting [parameterized UV variability based on observations in previous SCs (2)] shows similar results.

Although the differences could be partially caused by limitations in our current understanding of middle atmospheric $HO_x - O_3$ chemistry, the uncertainty in solar UV variability may be another major source. Haigh et al. (5) reported SORCE (SOLSTICE and SIM) SSI variability from April 2004 through November 2007, which is significantly larger than that of the NRL SSI and can better explain the observed atmospheric O_3 changes (5, 6, 8, 9). However, given the unexpected large discrepancies, whether SORCE SSI should be used in models has been hotly debated since then. Many remain skeptical about SORCE SSI, pending additional validation and future updates on the degradation correction of SORCE instruments (37, 38), whereas others conducted modified solar physics model parameterizations that agree better with SORCE data (39) and provided solar proxy evidence suggesting that the declining phase of SC 23 might be very different from previous SCs (40) (more details are provided in *SI Text*).

Therefore, it is important to investigate the sensitivity of the atmospheric OH SC signal to the large difference between NRL and SORCE SSI data. We repeat the WACCM simulation by replacing NRL SSI with SORCE SSI as the solar forcing. To mimic a full SC, SORCE SSI data are extrapolated back to the max of SC 23 in January 2002 using the Mg-II index as a proxy (*SI Text*). The resultant SSI variability and its comparison with NRL SSI are shown in Fig. 4 (*Inset*, showing an extrapolation scaling factor). The SORCE UV variability is generally larger than that from the NRL model. The relative difference is ~30% with the Lyman-α index (SOLSTICE data) and much larger (a factor of 2–6) at 200–280 nm (mainly SIM data). Considering the difference between SOLSTICE and SIM SSI data at 210–240 nm, we performed two WACCM runs using combined SSI variability from the two instruments with cutoffs at 240 nm and 210 nm, respectively. Fig. 3*C* shows the annual mean model X_{OH}

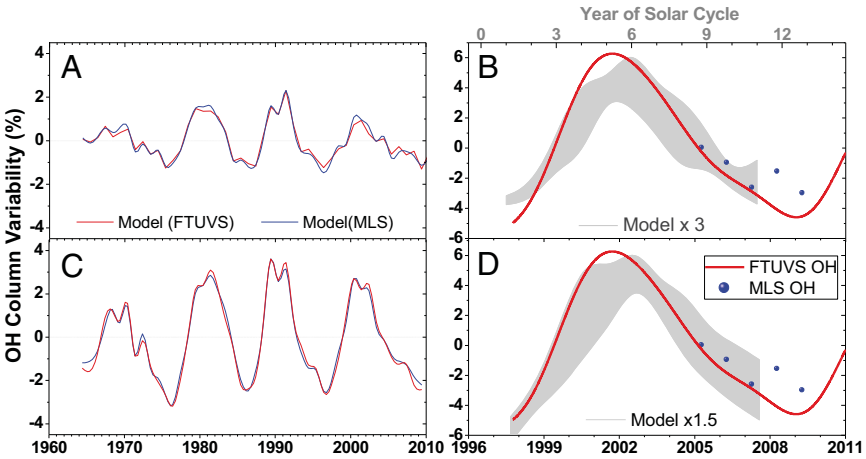

Fig. 3. Comparison of OH SC variabilities from the WACCM and observations. (*A*) Modeled variability of annual mean X_{OH} (using NRL SSI) integrated over the altitude ranges for FTUVS (red) and MLS (blue) X_{OH} values. (*B*) Model X_{OH} variability is increased by a factor of 3 (gray) to compare with observed X_{OH} SC signal (red and blue). The gray band indicates the scatter range of model X_{OH} variability over the simulated SCs. (*C* and *D*) Equivalent to *A* and *B* but for model results using SORCE SSI.

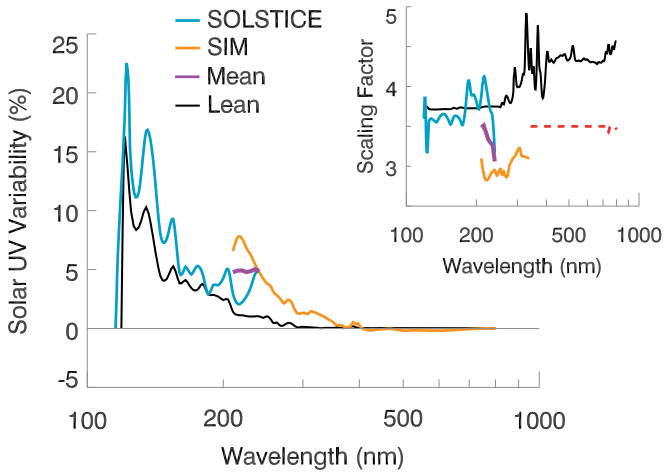

Fig. 4. Solar UV spectral variability derived from SORCE SSI. The blue and orange lines correspond to SSI data from the SOLSTICE and SIM, respectively. The purple line shows the mean of the two at 210–240 nm. The black line is the NRL SSI variation. All spectra have been convolved to the model grid. (*Inset*) Spectral scaling factors for extrapolating the observed SSI (April 2004–November 2007) to the solar max in January 2002. For values above 340 nm (not important for OH chemistry), an arbitrary factor of 3.5 is applied (dashed line).

using SORCE SSI variability (SOLSTICE, below 240 nm; SIM, above 240 nm). The X_{OH} SC variability is ~6% (twice that in Fig. 3*B*) and agrees much better with observations (10 ± 3% for the TMF, 7–8% for the MLS); the difference between the WACCM and TMF results is reduced to a factor of ~1.5 (Fig. 3*D*). The other WACCM run using 210 nm as the cutoff between SOLSTICE and SIM data gives a slightly larger X_{OH} variability of ~7%, closer to FTUVS results and agreeing well with MLS results. Additional SORCE SSI data covering the rising phase of SC 24 are needed before robust conclusions can be made.

To understand the detailed mechanism of the OH response to SC better, we use a 1D photochemical model (24, 25) to study vertical and spectral distribution of OH sensitivity to SSI changes. It has the advantages of much higher computational efficiency and flexibility than the WACCM, allowing for a wide range of sensitivity studies to elucidate the underlying mechanisms responsible for the OH response to SC. The spectral OH response, defined as the ratio of the relative change in model OH to the relative change in solar photon flux at the top of the atmosphere (%-[OH]/%-photon flux), highlights the important processes for OH photochemistry (Fig. 5*A*) as follows:

i) OH enhancements at 65–90 km and 50–80 km occur at the wavelengths of the Lyman-α index and at 170–200 nm, where direct H_2O photolysis is the major OH source.

ii) Positive OH responses at 210–340 nm correspond to enhanced O_3 photolysis, followed by enhanced OH production through the reaction of $O(^1D)$ (from O_3 photolysis) with H_2O.

iii) Negative OH responses above 80 km correspond to enhanced photolysis of O_2 (160–200 nm) and O_3 (255–290 nm), which produces atomic oxygen, a sink species for OH. This effect is insignificant in X_{OH} due to the very low OH abundance at these altitudes.

iv) Negative response at 190–220 nm below 40 km is caused by a shielding effect (17) resulting from UV attenuation by the enhanced overhead O_3 [O_3 at higher altitudes with a positive response to SC (5) absorbs more UV and diminishes the photolysis rates at lower altitudes]. It mostly cancels out effect of *ii* at these altitudes, leaving a small net negative response.

The vertical profile of model OH response to SC (Δ[OH]) (Fig. 5*B*) is obtained by convolving the spectral response in Fig. 5*A* with SSI variability (black, using the NRL; blue, using the SORCE). Earlier modeling work by Canty and Minschwaner (15) (orange) using solar forcing similar to that of the NRL is close to our model result using NRL SSI. Such Δ[OH] is the overall OH change due to changes in photolysis and OH sources/sinks. The Δ[OH] derived using SORCE SSI is generally larger than that using NRL SSI, owing to the greater solar UV variability from the SORCE. It is up to 18% at 70–80 km, near 5% at 40–60 km, and slightly negative at 30–40 km. In particular, by using SORCE SSI, OH SC signal increases by at least a factor of 2 at 40–60 km. This region of the atmosphere covers the primary OH density peak at ~45 km. Thus, the corresponding differences in SC signal in OH make large contributions to the difference in total OH column SC signal. The integrated X_{OH} response derived using NRL SSI is 3.7%; when SORCE SSI is used, the X_{OH} response increases to 6.4%. These values agree with those from the WACCM.

Implications

Catalytic O_3 loss above ~40 km is primarily controlled by HO_x reactions (16, 18, 19). O_3 in this region of the atmosphere is expected to show early signs of O_3 layer recovery (41) and has a strong impact on global stratospheric temperatures and circulation, and thus climate (42). Our findings of the OH response to SC have important implications for O_3 changes associated with HO_x variability. Previous studies of the O_3 response to SC (5, 6, 8, 9) are for the overall O_3 change (Δ[O_3]), including direct changes through photolysis, indirect changes through O_3-destroying catalysts (e.g., HO_x), and possible indirect changes through thermal structures and circulation [note that our WACCM model Δ[O_3] is

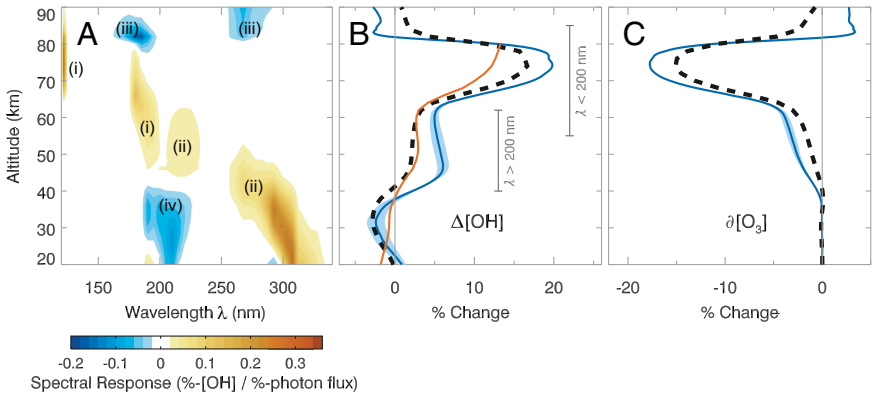

Fig. 5. Vertical profile of OH SC signal and its implications for O_3. (*A*) Spectral response of OH to changes in wavelength-resolved solar irradiance (the relative change in OH divided by the relative change in the photon flux) from the 1D model. The reference UV spectrum for perturbation is constructed with SOLSTICE data below 210 nm, SIM data above 240 nm, and the mean of SOLSTICE and SIM data at 210–240 nm when they disagree (Fig. 4). (*B*) Vertical profiles of OH SC signal from the model run using NRL SSI (black), using SORCE SSI (blue; shade representing the upper and lower limits of results derived using SOLSTICE or SIM data at 210–240 nm), and from Canty and Minschwaner (15) (orange). (*C*) Corresponding O_3 variability (solely due to the changes in OH in *B*).

very similar, if not identical, to $\Delta[O_3]$ from a previous study using the same model and similar SSI data from both the SORCE and NRL, in which the modeled $\Delta[O_3]$ using SORCE SSI agrees better with observations (6)]. It is important to quantify the impact of each individual process. Here, we discuss the component of $\Delta[O_3]$ that is solely due to $\Delta[OH]$ (denoted by $\partial[O_3]$). We made additional 1D model runs by constraining $\Delta[OH]$ to values from the runs performed above (using NRL and SORCE SSI data) and fixing UV flux (no other components of $\Delta[O_3]$). All species other than OH are allowed to vary until reaching steady state. The resultant O_3 change represents $\partial[O_3]$ (Fig. 5*C*). Above 60 km, $\partial[O_3] \approx -\Delta[OH]$ (15). The peak $\partial[O_3]$ at 75 km is −15% and −18% for the runs using $\Delta[OH]$ from NRL and SORCE SSI data, respectively. Below 40 km, $\partial[O_3]$ is negligibly small. At 40–60 km, using $\Delta[OH]$ from SORCE SSI instead of from NRL SSI leads to nearly doubled $\partial[O_3]$. Merkel et al. (6) showed that the WACCM modeled $\Delta[O_3]$ at 40–60 km increases from 0.5% to 1% when NRL SSI is replaced by SORCE SSI. Similar results are also obtained using other models (5, 8). These changes in $\Delta[O_3]$ at 40–60 km are close to that in $\partial[O_3]$ alone, suggesting that OH SC variability may be the dominant factor underlying the O_3 response to SC in the upper stratosphere. Although more quantitative diagnostic studies will help confirm this, it is likely that OH and its SC variability play a critical role in the decadal variation in upper stratospheric O_3, which has to be accurately described before quantitative conclusions on O_3 layer recovery can be made.

Concluding Remarks

Both 1D and WACCM models using NRL SSI produce an X_{OH} response to SC that is much smaller than the observed X_{OH} response at the TMF. Assuming that our current understanding of the $HO_x - O_3$ photochemistry system is complete, which may or may not be true, using SORCE SSI gives results much closer to observations. Thus, the uncertainty in SSI variability may be a primary limitation for accurate modeling of OH variability and the corresponding catalytic O_3 change. Although the NRL model could have underestimated the solar forcing in SC 23, several other factors involving the trends in OH sources/sinks could have contributed to the larger observed OH variability.

One candidate is the trend in atmospheric H_2O (43). Satellite and ground-based measurements revealed a decreasing trend of a few percentage points per year in H_2O at 16–26 km during 2000–2005 (43, 44). Remsberg (45) reported an increasing trend in mesospheric H_2O of ∼1% per year at 60–80 km. We approximated the H_2O trend at 26–60 km by linear interpolation and simulated the impact of these trends on OH using the 1D model (*SI Text*). The resulting change in X_{OH} is only −0.2% per year. In addition, after 2005, the H_2O trend switches from negative to positive (44), which does not contribute to the observed X_{OH} decrease during 2005–2009.

Similarly, a non-SC O_3 trend may also contribute to the observed X_{OH} change. A recent study using ground-based LIDAR (light detection and ranging) measurement over the TMF showed a ∼2% per decade O_3 trend at 35–45 km since 1997 (46). Trends at other altitudes are not available. Our 1D model sensitivity study suggests that a forced 1% per decade O_3 variability at all altitudes would lead to only a ∼0.04% per decade change in X_{OH}. Thus, the potential impact from the long-term non-SC O_3 trend is negligible. Observational evidence suggests that the O_3 SC variability is unlikely to exceed 10% (peak to valley) at all altitudes. Thus, the impact of decadal O_3 variability (SC and non-SC trends) has a minimal impact on OH column variability (within ∼0.4% per decade), whereas the OH SC change has a dominant impact on O_3 (see discussions on $\partial[O_3]$). This clearly indicates the great effectiveness of HO_x catalytic chemistry in controlling upper stratospheric O_3 loss.

Models using SORCE SSI variability produce an X_{OH} response (6–7%) that agrees much better with observed X_{OH} (∼10% from FTUVS, ∼7% from MLS). The remaining difference is within the uncertainty range of TMF X_{OH}, and it could also originate from the aforementioned small impacts of H_2O and O_3 trends. In addition, the extrapolated SORCE SSI variability in this study covers 2002 (max of SC 23) through 2007. The SSI in 2007 is reasonably close but might be slightly larger than the real SC min (2008–2009). This could also lead to a small underestimation in modeled OH SC signal. Updated SORCE SSI data in the future could help to confirm this.

Although models using SORCE SSI over SC 23 agree better with observations than models using NRL SSI, it is too early to conclude that climate models should switch from NRL SSI to SORCE SSI. Questions remain as to why SSI measurements during previous SCs did not show such large variability, whether SORCE SSI variability is applicable to other SCs, whether the difference is at least partially due to possible shortcomings in the NRL model and/or degradation in the SORCE instruments, and whether our current understanding of middle atmospheric $HO_x - O_3$ chemistry is complete.

In any case, continuous long-term observations of solar SSI, OH, O_3, and other related chemical species through SC 24 are crucial for further investigations to solve the above puzzles. Although MLS OH observations were temporarily suspended at the end of 2009 to extend the instrument's lifetime, month-long measurements in each summer over the next few years are planned to cover the peak of SC 24. These extended MLS OH data will be available after careful degradation corrections and validation. This unique dataset, in combination with the continuous ground-based FTUVS measurements, will provide valuable information about the global and vertical distribution of the SC signal in OH. The latter, with an accurately measured SSI variability, can rigorously test the photochemical mechanisms in current models.

Methods

FTUVS OH Data. The ground-based FTUVS at the TMF measures X_{OH} under clear to lightly cloudy conditions. The major systematic error is the uncertainty in the OH line center absorption cross-section (within 10%). The precision uncertainty of the daily max OH is estimated to be 3–5%. The complete diurnal measurement data have been archived at the Aura Validation Data Center (AVDC) of the Goddard Space Flight Center (http://avdc.gsfc.nasa.gov/). Any interested users may request an account through the Web site to download the data. The interpolated daily max OH data (after gap filling) used for FFT analysis in this study are provided in Dataset S1. More details about data interpolation and trend analysis are also provided in *SI Text*.

MLS OH Data. MLS OH data used in this study are from v3.3 retrieval software. We use data at 21.5–0.0032 hPa to calculate the OH column. The systematic uncertainty is within 8% over this pressure range (30). The zonal mean around the TMF (29.5° N, 39.5° N) is used. A similar analysis using data from a 10° × 25° grid box at the TMF was also performed. The results are similar to those presented here.

SORCE Solar Spectral Data. The SOLSTICE measurement (22) has a spectral resolution of 0.1 nm. The SIM measurement (23) has varying spectral resolution (∼1 nm in the UV setting). The SOLSTICE SSI data used in our models are from v10 retrieval software. A newer v11 version was released during the review process of this paper. A 1D model sensitivity study between v10 and v11 shows no significant impact on OH results. The ongoing degradation correction studies on SIM data are not expected to affect the SSI variability between 2004 and 2007. Details on the data quality and the derivation of the SSI variability for model simulations are included in *SI Text*.

WACCM Model. The WACCM uses the Model for Ozone and Related Chemical Tracers version 3 (MOZART3) as the chemical mechanism (2). Chemical species are all allowed to vary during model runs. For each UV setting, the model is run from 1960 to 2010. The first 4 y are ignored to allow model spin-up. We use the monthly mean output to derive the OH SC signal. We also generated daily max outputs during the solar max year and solar min year to compare with results using the monthly mean. The difference was found to be very small.

1D Model. The 1D model is a California Institute of Technology/JPL photochemical model that includes over 100 chemical species, over 460 reactions, vertical transport (eddy, molecular, and thermal diffusion), and coupled radiative transfer (23). The chemical kinetics have been updated to JPL06-2 (47). A more recent update of JPL10-6 (48) does not introduce significant differences on reactions related to HO_x chemistry. Sixty-five layers are used to cover from the ground to 130 km. OH fluxes at the surface and the top of the atmosphere are fixed as zero. During model runs, chemical species are not constrained unless otherwise stated. The temperature profile is fixed. The model has been applied to study the diurnal cycle of OH (49). Typical model profiles of OH, O_3, and related species are shown in *SI Text*.

ACKNOWLEDGMENTS. We thank the NASA Aura Science Team and the Upper Atmosphere Research and Tropospheric Chemistry programs for their support. We thank R. C. Willson for providing the ACRIM TSI composite (www.acrim.com) and the Laboratory for Atmospheric and Space Physics Interactive Solar Irradiance Datacenter for composites of Lyman-α and Mg-II indices (http://lasp.colorado.edu/lisird/). We also acknowledge receipt of a TSI dataset from the PMOD (www.pmodwrc.ch/) and receipt of unpublished data from the Variability of Solar Irradiance and Gravity Oscillations on board the Solar and Heliospheric Observatory. Some FTUVS OH data from early years were collected by R. P. Cageao. We thank H. M. Pickett, the principal investigator (retired) for the MLS OH measurements and a NASA Aura Science Team project. We also thank R.-L. Shia and S. Newman for help with the models and error analysis and insightful discussions. Work at the Jet Propulsion Laboratory, California Institute of Technology, was done under contract to NASA. Support from an Australian Research Council Linkage International grant is gratefully acknowledged.

1. Gray LJ, et al. (2010) Solar influences on climate. *Rev Geophys* 48(4):RG4001, 10.1029/2009RG000282.
2. Marsh DR, et al. (2007) Modeling the whole atmosphere response to solar cycle changes in radiative and geomagnetic forcing. *J Geophys Res Atmos* 112:D23306, 10.1029/2006JD008306.
3. Beig G, et al. (2012) Inter-comparison of 11-year solar cycle response in mesospheric ozone and temperature obtained by HALOE satellite data and HAMMONIA model. *J Geophys Res Atmos* 117:D00P10, 10.1029/2011JD015697.
4. Soukharev BE, Hood LL (2006) Solar cycle variation of stratospheric ozone: Multiple regression analysis of long-term satellite data sets and comparisons with models. *J Geophys Res Atmos* 111:D2031410.1029/2006JD007107.
5. Haigh JD, Winning AR, Toumi R, Harder JW (2010) An influence of solar spectral variations on radiative forcing of climate. *Nature* 467(7316):696–699, 10.1038/nature09426.
6. Merkel AW, et al. (2011) The impact of solar spectral irradiance variability on middle atmospheric ozone. *Geophys Res Lett* 38:L13802, 10.1029/2011GL047561.
7. Randel WJ, Wu F (2007) A stratospheric ozone profile data set for 1979-2005: Variability, trends, and comparisons with column ozone data. *J Geophys Res Atmos* 112: D06313, 10.1029/2006JD007339.
8. Swartz WH, et al. (2012) Middle atmosphere response to different descriptions of the 11-yr solar cycle in spectral irradiance in a chemistry-climate model. *Atmos Chem Phys* 12:5937–5948, 10.5194/acp-12-5937-2012.
9. Li K-F, et al. (2012) Simulation of solar-cycle response in tropical total column ozone using SORCE irradiance. *Atmospheric Chemistry and Physics Discussions* 12:1867–1893, 10.5194/acpd-12-1867-2012.
10. Hood LL, et al. (2010) Decadal variability of the tropical stratosphere: Secondary influence of the El Niño-Southern Oscillation. *J Geophys Res Atmos* 115:D11113, 10.1029/2009JD012291.
11. Matthes K, et al. (2010) Role of the QBO in modulating the influence of the 11 year solar cycle on the atmosphere using constant forcings. *J Geophys Res Atmos* 115: D18110, 10.1029/2009JD013020.
12. Austin J, et al. (2008) Coupled chemistry climate model simulations of the solar cycle in ozone and temperature. *J Geophys Res Atmos* 113:D11306, 10.1029/2007JD009391.
13. Brasseur GP (1993) The response of the middle atmosphere to long-term and short-term solar variability: A 2-dimensional model. *J Geophys Res Atmos* 98:23079–23090, 10.1029/93JD02406.
14. Sandor BJ, Clancy RT (1998) Mesospheric HO_x chemistry from diurnal microwave observations of HO_2, O_3, and H_2O. *J Geophys Res Atmos* 103:13337–13351, 10.1029/98JD00432.
15. Canty T, Minschwaner K (2002) Seasonal and solar cycle variability of OH in the middle atmosphere. *J Geophys Res Atmos* 107:4737, 10.1029/2002JD002278.
16. McElroy MB, Salawitch RJ (1989) Changing composition of the global stratosphere. *Science* 243(4892):763–770, 10.1126/science.243.4892.763.
17. Mills FP, et al. (2003) OH column abundance over Table Mountain Facility, California: Intra-annual variations and comparisons to model predictions for 1997-2001. *J Geophys Res Atmos* 108:4785, 10.1029/2003JD003481.
18. Osterman GB, et al. (1997) Balloon-borne measurements of stratospheric radicals and their precursors: Implications for the production and loss of ozone. *Geophys Res Lett* 24:1107–1110, 10.1029/97GL00921.
19. Salawitch RJ, et al. (2005) Sensitivity of ozone to bromine in the lower stratosphere. *Geophys Res Lett* 32:L05811, 10.1029/2004GL021504.
20. Pickett HM, Peterson DB (1996) Comparison of measured stratospheric OH with prediction. *J Geophys Res Atmos* 101:16789–16796, 10.1029/96JD01168.
21. Snow M, et al. (2005) Solar-Stellar Irradiance Comparison Experiment II (SOLSTICE II): Examination of the solar-stellar comparison technique. *Sol Phys* 230:295–324, 10.1007/s11207-005-8763-3.
22. Harder JW, et al. (2010) The SORCE SIM solar spectrum: Comparison with recent observations. *Sol Phys* 263:3–24, 10.1007/s11207-010-9555-y.
23. Allen M, et al. (1981) Vertical Transport and Photochemistry in the Terrestrial Mesosphere and Lower Thermosphere (50-120 km). *J Geophys Res -Space Phys* 86: 3617–3627, 10.1029/JA086iA05p03617.
24. Cageao RP, et al. (2001) High-Resolution Fourier-Transform Ultraviolet-Visible Spectrometer for the Measurement of Atmospheric Trace Species: Application to OH. *Appl Opt* 40(12):2024–2030, 10.1364/AO.40.002024.
25. Minschwaner K, et al. (2003) Hydroxyl column abundance measurements: PEPSIOS instrumentation at the Fritz Peak Observatory and data analysis techniques. *J Atmos Sol Terr Phys* 65:335–344, 10.1016/S1364-6826(02)00297-3.
26. Li K-F, et al. (2005) OH column abundance over Table Mountain Facility, California: AM-PM diurnal asymmetry. *Geophys Res Lett* 32:L13813, 10.1029/2005GL022521.
27. Mills FP, et al. (2002) OH column abundance over Table Mountain Facility, California: Annual average 1997-2000. *Geophys Res Lett* 29:1742, 10.1029/2001GL014151.
28. Pickett HM (2006) Microwave Limb Sounder THz module on Aura. *IEEE Trans Geosci Remote Sens* 44:1122–1130, 10.1109/TGRS.2005.862667.
29. Canty T, et al. (2006) Stratospheric and mesospheric HO_x: Results from aura MLS and FIRS-2. *Geophys Res Lett* 33:L12802, 10.1029/2006GL025964.
30. Pickett HM, et al. (2008) Validation of aura microwave limb sounder OH and HO_2 measurements. *J Geophys Res Atmos* 113:D16S30, 10.1029/2007JD008775.
31. Wang S, et al. (2008) Validation of aura microwave limb dounder OH measurements with Fourier transform ultra-violet spectrometer total OH column measurements at Table Mountain, California. *J Geophys Res Atmos* 113:D22301, 10.1029/2008JD009883.
32. Scafetta N, Willson RC (2009) ACRIM-gap and TSI trend issue resolved using a surface magnetic flux TSI proxy model. *Geophys Res Lett* 36:L05701, 10.1029/2008GL036307.
33. Fröhlich C (2006) Solar irradiance variability since 1978—Revision of the PMOD composite during solar cycle 21. *Space Sci Rev* 125:53–65, 10.1007/s11214-006-9046.
34. Kopp G, et al. (2005) The Total Irradiance Monitor (TIM): Science results. *Sol Phys* 230: 129–139, 10.1007/s11207-005-7433-9.
35. Kopp G, Lean JL (2011) A new, lower value of total solar irradiance: Evidence and climate significance. *Geophys Res Lett* 38:L01706, 10.1029/2010GL045777.
36. Lean JL, et al. (1997) Detection and parameterization of variations in solar mid- and near-ultraviolet radiation (200-400 nm). *J Geophys Res Atmos* 102:29939–29956, 10.1029/97JD02092.
37. Lean JL, DeLand MT (2012) How does the Sun's spectrum vary? *J Clim* 25:2555–2560.
38. DeLand MT, Cebula RP (2012) Solar UV variations during the decline of Cycle 23. *J Atmos Sol Terr Phys* 77:225–234.
39. Fontenla JM, et al. (2011) High-resolution solar spectral irradiance from extreme ultraviolet to far infrared. *J Geophys Res* 116:D20108, 10.1029/2011JD016032.
40. Lukianova R, Mursula K (2011) Changed relation between sunspot numbers, solar UV/EUV radiation and TSI during the declining phase of solar cycle 23. *J Atmos Sol Terr Phys* 73:235–240.
41. Newchurch MJ, et al. (2003) Evidence for slowdown in stratospheric ozone loss: First stage of ozone recovery. *J Geophys Res Atmos* 108:4507, 10.1029/2003JD003471.
42. Müller R, Salawitch RJ (1999) Upper stratospheric processes. *Scientific Assessment of Ozone Depletion: 1998, WMO Global Ozone Research and Monitoring Project—Report No. 44* (World Meteorological Organization, Geneva), pp 6.1–6.44.
43. Solomon S, et al. (2010) Contributions of stratospheric water vapor to decadal changes in the rate of global warming. *Science* 327(5970):1219–1223, 10.1126/science.1182488.
44. Hurst DF, et al. (2011) Stratospheric water vapor trends over Boulder, Colorado: Analysis of the 30-year Boulder record. *J Geophys Res Atmos* 116:D02306, 10.1029/2010JD015065.
45. Remsberg E (2010) Observed seasonal to decadal scale responses in mesospheric water vapor. *J Geophys Res Atmos* 115:D06306, 10.1029/2009JD012904.
46. Steinbrecht W, et al. (2006) Long-term evolution of upper stratospheric ozone at selected stations of the Network for the Detection of Stratospheric Change (NDSC). *J Geophys Res Atmos* 111:D10308, 10.1029/2005JD006454.
47. Sander SP, et al. (2006) *Chemical Kinetics and Photochemical Data for Use in Atmospheric Studies Evaluation No. 15, Technical Report JPL Publication 06-2* (Jet Propulsion Laboratory, Pasadena, CA).
48. Sander SP, et al. (2011) *Chemical Kinetics and Photochemical Data for Use in Atmospheric Studies Evaluation No. 17, Technical Report JPL Publication 10-6* (Jet Propulsion Laboratory, Pasadena, CA).
49. Pickett HM, et al. (2006) Observation of night OH in the mesosphere. *Geophys Res Lett* 33:L19808, 10.1029/2006GL026910.